Supplementary Information

Realization of high-temperature metallic altermagnetism in transition metal graphite intercalation compounds

Xiaojun He,[a†] Guo-Dong Zhao, [b†] Weida Fu,[a] Tao Hu,*[a] Wencai Yi,[d] Hui Zhang,[b] Xiaonong Shen,[b] Alessandro Stroppa,[c] Wei Ren [b] and Zhongming Ren [a]

[a]School of Materials Science and Engineering, State Key laboratory of Advanced Special Steel, Shanghai University, Shanghai, 200241, China

[b]Department of Physics, Materials Genome Institute, International Centre for Quantum and Molecular Structures, Shanghai University, Shanghai 200444, China

[c]CNR-SPIN c/o Università degli Studi dell'Aquila, Via Vetoio 10, I-67010 Coppito (L'Aquila), Italy

[d]Laboratory of High Pressure Physics and Material Science, School of Physics and Physical Engineering, Qufu Normal University, Qufu 273165, China

* Corresponding author: taohu@shu.edu.cn (T. Hu)

Table S1

The table lists the magnetic ground states for transition metals (TMs) at various intercalation sites (HH, NH, and TS). ΔE denotes the energy difference between the AFM and FM states in meV.

TM	Ueff (eV)		Intercalation site		
			HH	NH	TS
Cr	3.4	Magnetic ground state	FM	AFM	AFM
		ΔE (meV)	378	345	14
Mn	4.8	Magnetic ground state	FM	FM	FM
		ΔE (meV)	66	246	90
Fe	5.1	Magnetic ground state	FM	FM	AFM
		ΔE (meV)	100	980	114
Co	6.2	Magnetic ground state	FM	NM	AFM
		ΔE (meV)	21	\	50

Table S2

Calculated properties of V-GICs under different intercalation concentrations and atomic distributions. This table summarizes the evolution of magnetic ground states, symmetry, and electronic properties across various concentrations (50%, 25%, 12.5%, 6.25%, and 5.56%).

Concentration	Magnetic ground state	Space group	Magnetic moment (μ_B)	Relative energy (eV/atom)
50%	AM	$P6_3mc$	1.49	1.602
25%	FM	$Pmn2_1$	1.57	0.975
12.5%	AM	$P6_3mc$	2.63	0.355
6.25%	AFM	$P3m1$	2.36	0.058
5.56%	AM	$P6_3mc$	2.71	0

To investigate the concentration-dependent electronic and magnetic properties of V-intercalated graphite, we strategically selected several discrete concentrations (50%, 25%, 12.5%, 6.25%, and 5.56%) based on structural symmetry and model feasibility (Fig. S2). The 12.5% concentration corresponds to the primary system investigated in the main artical. For concentrations of 50%, 6.25%, and 5.56%, the vanadium atoms are positioned at sites analogous to the HH configuration, which preserves the intrinsic hexagonal symmetry of the pristine graphite lattice. In contrast, the 25% concentration adopts a configuration similar to the NH configuration. While the 50%, 25%, and 5.56% configurations theoretically possess the structural symmetry compatible with AM, the 6.25% concentration fails to maintain the necessary symmetry to support an AM phase, resulting in its convergence to an AFM ground state. Among the viable candidates, the 25% concentration ultimately favors a FM ground state. Furthermore, the remaining 50% and 5.56% configurations represent two extremes of the trade-off between magnetic splitting and energetic stability. Specifically, while the 50% concentration exhibits a substantial conduction band splitting of up to 477 meV due to the high density and proximity of V atoms (Fig. S3), its excessively high relative energy renders it thermodynamically unfavorable. Conversely, while the 5.56% concentration achieves the lowest relative energy, the increased interatomic distance significantly weakens the magnetic exchange interaction, leading to a diminished maximum splitting of 122 meV. Consequently, the 12.5% concentration strikes an optimal balance. It maintains robust magnetic exchange and a significant spin splitting while ensuring structural symmetry and energetic viability, thus emerging as the ideal candidate for realizing the AM phase.

Table S3

Symmetry analysis and magnetic properties of the altermagnetic ground state of the HH configuration (*P6₃mc*, No. 186). The table lists the Wyckoff position, site symmetry, and local magnetic moment (μ_B) for each atomic site.

Atom	Site symmetry	Fractional Coordinates (*x*, *y*, *z*)	Magnetic moment (μ_B)
C_1 (2a)	3m.	(0.000, 0.000, 0.262)	-0.095
C_2 (2a)	3m.	(0.000, 0.000, 0.762)	0.095
C_3 (6c)	.m.	(0.330, 0.165, 0.253)	0.066
C_4 (6c)	.m.	(0.165, 0.330, 0.753)	-0.066
C_5 (6c)	.m.	(0.500, -0.001, 0.246)	0.022
C_6 (6c)	.m.	(0.500, 0.001, 0.746)	-0.022
C_7 (6c)	.m.	(0.835, 0.165, 0.253)	0.066
C_8 (2b)	3m.	(0.667, 0.333, 0.761)	0.093
C_9 (6c)	.m.	(0.001, 0.500, 0.246)	0.022
C_{10} (6c)	.m.	(-0.001, 0.500, 0.746)	-0.022
C_{11} (2b)	3m.	(0.333, 0.667, 0.261)	-0.093
C_{12} (6c)	.m.	(0.165, 0.835, 0.753)	-0.066
C_{13} (6c)	.m.	(0.500, 0.500, 0.250)	0.022
C_{14} (6c)	.m.	(0.500, 0.500, 0.750)	-0.022
C_{15} (6c)	.m.	(0.835, 0.670, 0.253)	0.066
C_{16} (6c)	.m.	(0.670, 0.835, 0.753)	-0.066
V_1 (2b)	3m.	(0.333, 0.667, -0.021)	2.638
V_2 (2b)	3m.	(0.667, 0.333, 0.479)	-2.638

Table S4

Symmetry analysis and magnetic properties of the altermagnetic ground state of the NH configuration (*Aem2*, No. 39). The table lists the Wyckoff position, site symmetry, and local magnetic moment (μ_B) for each atomic site.

Atom	Site symmetry	Fractional Coordinates (*x*, *y*, *z*)	Magnetic moment (μ_B)
C_1 (4c)	.m.	(0.250, 0.250, 0.493)	-0.010
C_2 (4c)	.m.	(0.250, 0.250, 0.005)	0.115
C_3 (8d)	1	(0.000, 0.668, 0.500)	0.000
C_4 (8d)	1	(0.250, 0.084, 0.998)	-0.087
C_5 (4c)	.m.	(0.250, 0.750, 0.507)	0.010
C_6 (4c)	.m.	(0.250, 0.750, 0.995)	-0.115
C_7 (8d)	1	(0.500,0.668, 0.500)	0.000
C_8 (8d)	1	(0.250, 0.584, 0.002)	0.087
C_9 (8d)	1	(0.500, 0.501, 0.500)	0.000
C_{10} (8d)	1	(0.500, 0.501, 0.000)	0.000
C_{11} (8d)	1	(0.250, 0.916, 0.488)	-0.098
C_{12} (8d)	1	(0.000, 0.833, 0.000)	0.000
C_{13} (4a)	..2	(0.000, 0.500, 0.500)	0.000
C_{14} (4a)	..2	(0.000, 0.500, 0.000)	0.000
C_{15} (8d)	1	(0.250, 0.416, 0.512)	0.098
C_{16} (8d)	1	(0.500, 0.833, 0.000)	0.000
C_{17} (4c)	.m.	(0.750, 0.750, 0.493)	-0.010
C_{18} (4c)	.m.	(0.750, 0.750, 0.005)	0.115
C_{19} (8d)	1	(0.500, 0.168, 0.500)	0.000
C_{20} (8d)	1	(0.750, 0.584, 0.998)	-0.087
C_{21} (4c)	.m.	(0.750, 0.250, 0.507)	0.010
C_{22} (4c)	.m.	(0.750, 0.250, 0.995)	-0.115
C_{23} (8d)	1	(0.000, 0.168, 0.500)	0.000
C_{24} (8d)	1	(0.750, 0.084, 0.002)	0.087
C_{25} (4a)	..2	(0.000, 0.001, 0.500)	0.000
C_{26} (4a)	..2	(0.000, 0.001, 0.000)	0.000
C_{27} (8d)	1	(0.750, 0.416, 0.488)	-0.098
C_{28} (8d)	1	(0.500, 0.333, 0.000)	0.000
C_{29} (4b)	..2	(0.500, 0.001, 0.500)	0.000
C_{30} (4b)	..2	(0.500, 0.001, 0.000)	0.000
C_{31} (8d)	1	(0.750, 0.916, 0.512)	0.098
C_{32} (8d)	1	(0.000, 0.333, 0.000)	0.000
V_1 (8d)	1	(0.250, 0.914, 0.767)	2.505
V_2 (8d)	1	(0.250, 0.414, 0.233)	-2.505
V_3 (8d)	1	(0.750, 0.414, 0.767)	2.505
V_4 (8d)	1	(0.750, 0.914, 0.233)	-2.505

Table S5

Symmetry operations of the space group *P6$_3$mc* [1,2], listed using Seitz symbols. Among them, 1 and -1 denotes identity and inversion, respectively. The operation 6_{001} denotes a sixfold rotation around the [001] axis, with 6^+ signifying a clockwise rotation and 6^- denoting counterclockwise rotation. m_{100} represents a mirror reflection with the (100) plane as the mirror plane. Vectors such as $[00\frac{1}{2}]$ denote glide translation (*t*). Other operations follow similar conventions.

$\{1 \mid 0\}$	: (*a*, *b*, *c*) →(*a*, *b*, *c*)	$\{m_{110} \mid 0\}$	: (*a*, *b*, *c*) → (-*b*, -*a*, *c*)
$\{3^+_{001} \mid 0\}$	: (*a*, *b*, *c*) → (-*b*, *a*-*b*, *c*)	$\{m_{100} \mid 0\}$	: (*a*, *b*, *c*) → (-*a*+*b*, *b*, *c*)
$\{3^-_{001} \mid 0\}$	: (*a*, *b*, *c*) → (-*a*+*b*, - *a*, *c*)	$\{m_{010} \mid 0\}$	: (*a*, *b*, *c*) → (*a*, *a*-*b*, *c*)
$\{2_{001} \mid 00\frac{1}{2}\}$	: (*a*, *b*, *c*) → (-*a*, -*b*, *c*+$\frac{1}{2}$)	$\{m_{1\bar{1}0} \mid 00\frac{1}{2}\}$	: (*a*, *b*, *c*) → (*b*, *a*, *c*+$\frac{1}{2}$)
$\{6^+_{001} \mid 00\frac{1}{2}\}$	: (*a*, *b*, *c*) → (*a*-*b*, *a*, *c*+$\frac{1}{2}$)	$\{m_{120} \mid 00\frac{1}{2}\}$	: (*a*, *b*, *c*) → (*a*-*b*, -*b*, *c*+$\frac{1}{2}$)
$\{6^-_{001} \mid 00\frac{1}{2}\}$	: (*a*, *b*, *c*) → (*b*, -*a*+*b*, *c*+$\frac{1}{2}$)	$\{m_{210} \mid 00\frac{1}{2}\}$	: (*a*, *b*, *c*) → (-*a*, -*a*+*b*, *c*+$\frac{1}{2}$)

Table S6

Symmetry operations of the space group *Aem2* [1,2], listed using Seitz symbols.

$\{1 \mid 0\}$	: (*a*, *b*, *c*) →(*a*, *b*, *c*)	$\{2_{001} \mid 0\}$	: (*a*, *b*, *c*) →(-*a*, -*b*, *c*)
$\{1 \mid 0\frac{11}{22}\}$	: (*a*, *b*, *c*) →(*a*, *b*+$\frac{1}{2}$, *c*+$\frac{1}{2}$)	$\{2_{001} \mid 0\frac{11}{22}\}$	: (*a*, *b*, *c*) →(-*a*, -*b*+$\frac{1}{2}$, *c*+$\frac{1}{2}$)
$\{m_{010} \mid 00\frac{1}{2}\}$	: (*a*, *b*, *c*) →(*a*, -*b*, *c*+$\frac{1}{2}$)	$\{m_{100} \mid 00\frac{1}{2}\}$	: (*a*, *b*, *c*) →(-*a*, *b*, *c*+$\frac{1}{2}$)
$\{m_{010} \mid 0\frac{1}{2}0\}$	: (*a*, *b*, *c*) →(*a*, -*b*+$\frac{1}{2}$, *c*)	$\{m_{100} \mid 0\frac{1}{2}0\}$	: (*a*, *b*, *c*) →(-*a*, *b*+$\frac{1}{2}$, *c*)

Table S7

Sensitivity analysis of the magnetic and electronic properties of V-GICs with respect to U_{eff}. The table summarizes the calculated energy difference between the antiferromagnetic (altermagnetic for HH and NH) and ferromagnetic phases, the local magnetic moment of vanadium atoms, the maximum spin-splitting energy of the conduction bands and MAE for U_{eff} values ranging from 3.0 to 6.0 eV. ΔE denotes the relative energy difference per atom among the three different intercalation sites at each U_{eff}.

Intercalation site	U_{eff} (eV)	3	4	5	6
HH	E_{FM} - E_{AFM}(meV)	459	378	284	194
	Magnetic Moment (μ_B)	2.49	2.52	2.63	2.60
	Max band splitting (meV)	235	306	272	239
	MAE (meV)	0.4	0.5	0.6	0.7
	ΔE (meV/atom)	3.1	0	3.3	15.3
NH	E_{FM} - E_{AFM}(meV)	394	429	421	402
	Magnetic Moment (μ_B)	2.28	2.41	2.50	2.57
	Max band splitting (meV)	122	159	201	236
	MAE (meV)	0.4	0.5	0.6	0.7
	ΔE (meV/atom)	0	0.4	3.9	18.6
TS	E_{FM} - E_{AFM} (meV)	118	139	143	292
	Magnetic Moment (μ_B)	2.54	2.58	2.61	2.64
	ΔE (meV/atom)	29.7	12.5	0	0

To confirm the reliability of our conclusions, we performed a sensitivity analysis by varying the U_{eff} parameter from 3.0 to 6.0 eV. The results demonstrate that the qualitative physical picture of V-GICs remains remarkably robust across this range. Specifically, for all considered U_{eff} values, the $E_{FM} - E_{AFM}$ values stay positive, indicating that the altermagnetic or antiferromagnetic ground states are energetically more favorable than the ferromagnetic phase in $C_{16}V_2$. However, the relative energy difference ΔE among the three intercalation sites exhibits strong U_{eff} dependence.

Therefore, we further verified their structural stability using phonon dispersion and AIMD calculations (Fig. 2). The TS configuration is ruled out due to the presence of large imaginary frequencies in its phonon spectra. For the remaining stable HH and NH configurations, the considerable spin-splitting is consistently preserved across all U_{eff} values (Fig. S6). Furthermore, the MAE shows no sign of easy-axis switching. The HH configuration maintains a stable in-plane anisotropy, while the NH configuration exhibits persistent out-of-plane anisotropy. Although the magnitudes of magnetic moments, spin-splitting, and MAE values change slightly with U_{eff} due to the enhanced electron localization, the overall physical trends and the symmetry-dictated properties remain unchanged, justifying the choice of U_{eff} in our main study.

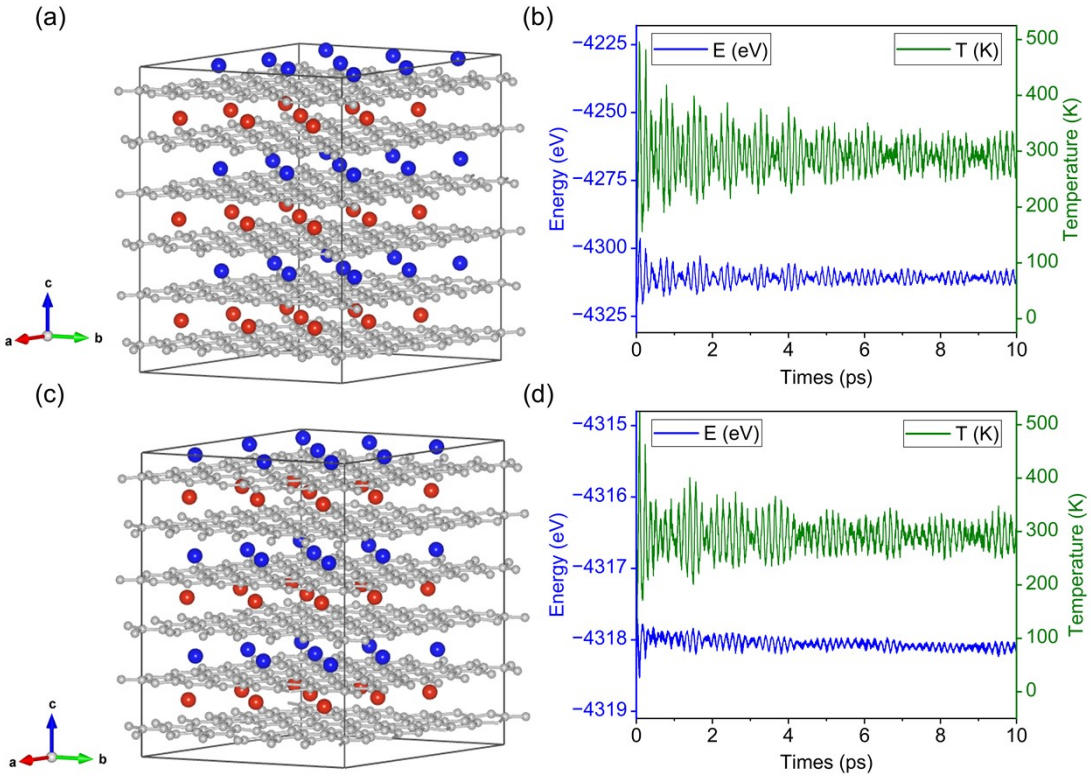

Fig. S1. Thermal stability of V-intercalated graphite at 300 K. (a, c) Perspective views of the 3×3×3 supercells containing 486 atoms for the (a) HH and (c) NH intercalation configurations after 10 ps of AIMD simulations at 300 K. Both configurations demonstrate structural integrity and relaxation to thermodynamic equilibrium. (b, d) Time evolution profiles of temperature fluctuations (green curves) and total energy convergence (blue curves) during the AIMD simulations for the (b) HH and (d) NH configurations, respectively.

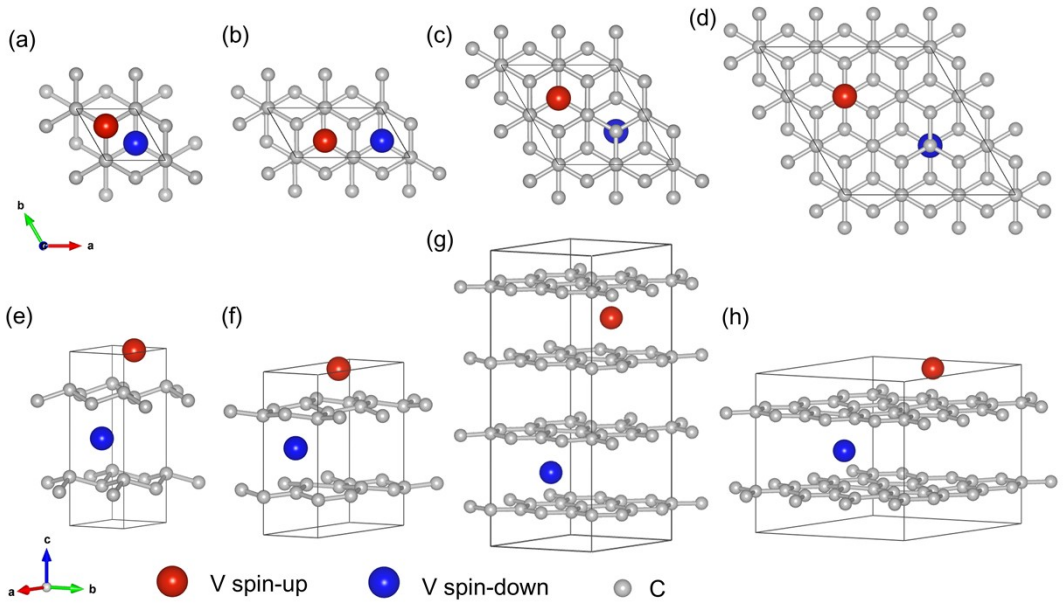

Fig. S2. Schematic crystal structures of V-GICs at various intercalation concentrations. (a)−(d) Top views along the *c*-axis and (e)−(h) corresponding perspective views for: (a, e) 50% concentration, a high-density stage-1 structure where V atoms occupy all available hexagonal centers in a 1×1×1 manner. (b, f) 25% concentration, a NH-like clustered distribution, showing decreased V−V proximity within a 2×1×1 supercell. (c, g) 6.25% concentration, a stage-2 structure featuring a HH-like uniform distribution in the *ab*-plane projection. (d, h) 5.56% concentration, a low-density 3×3×1 stage-1 structure representing the most uniform distribution, where the increased V−V distance leads to weakened exchange interactions.

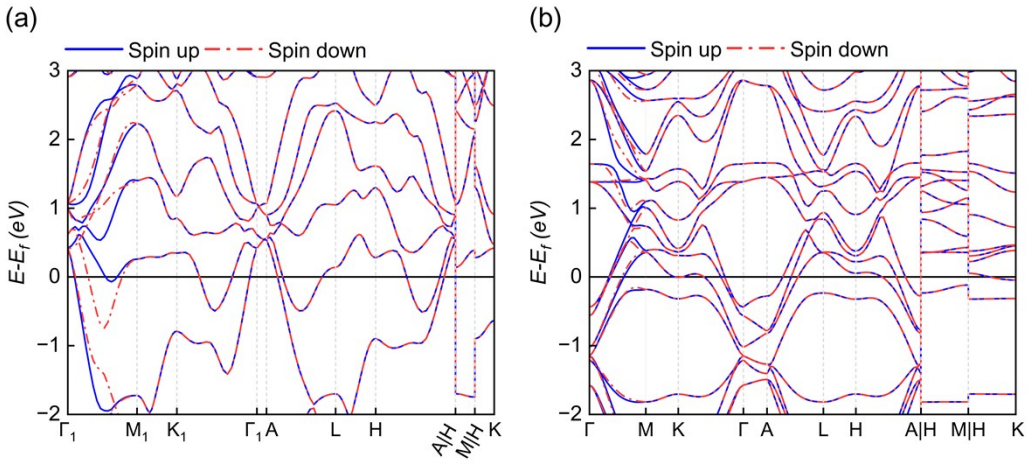

Fig. S3. Electronic band structures with different intercalation concentrations along the same high-symmetry path as the 12.5% HH phase for (a) 50% and (b) 5.56%.

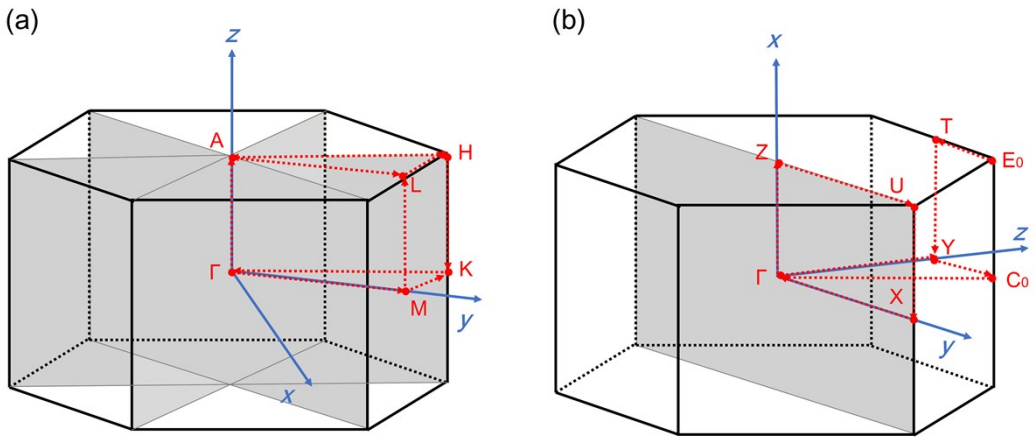

Fig. S4. The first Brillouin zone along with the high-symmetry *k*-path used in the band structure calculations of V-GICs for the (a) HH and (b) NH configurations, respectively.

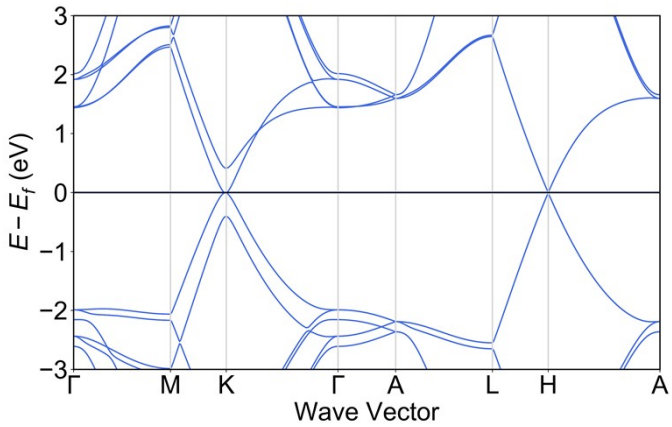

Fig. S5. Band structure of the pristine graphite, shown for reference. Our result excellently agrees with previous work [3].

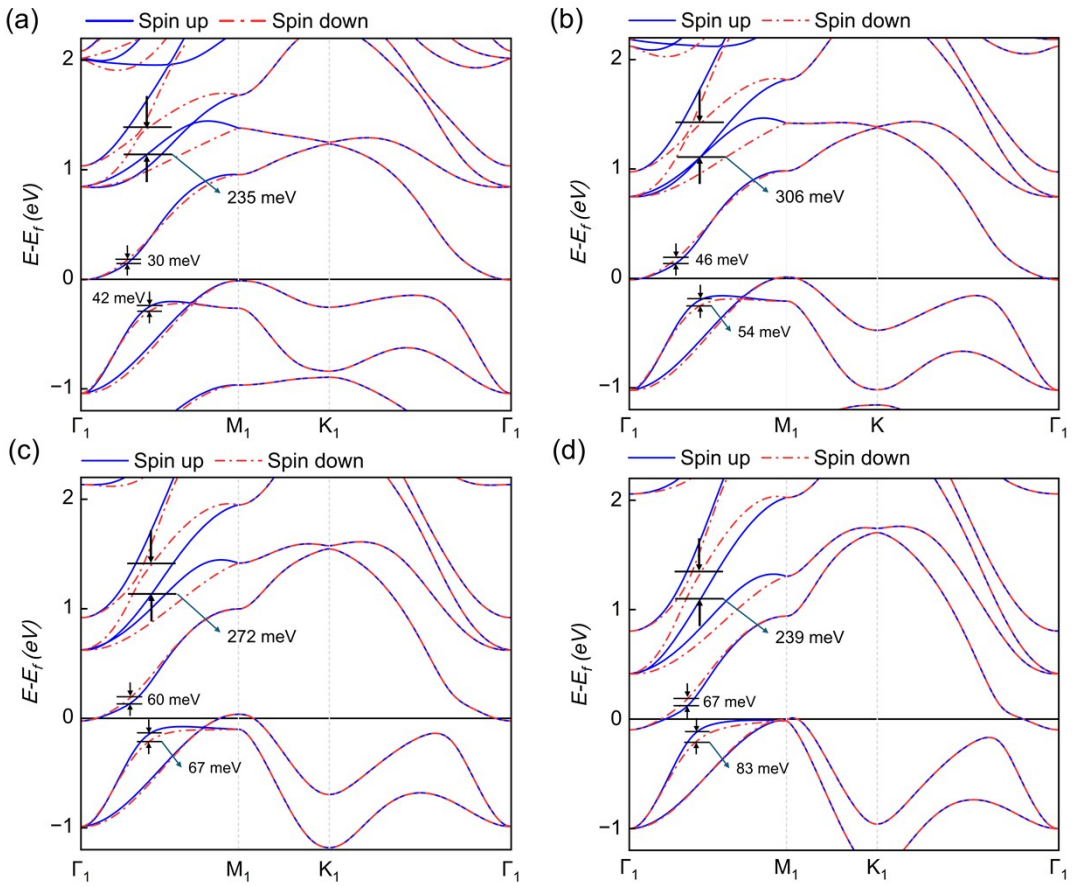

Fig. S6. Calculated band structures of the HH configuration under different U_{eff} corrections along the specific high-symmetry path **$\Gamma_1 - M_1 - K_1 - \Gamma_1$**: (a) U_{eff} = 3.0 eV, (b) 4.0 eV, (c) 5.0 eV, and (d) 6.0 eV. The red and blue lines represent spin-up and spin-down channels, respectively. Selected spin-splitting values near the conduction band minimum are explicitly marked. The comparison reveals that while the exact magnitude of the splitting varies slightly, the characteristic momentum-dependent splitting pattern and the metallic nature remain qualitatively consistent across the tested range.

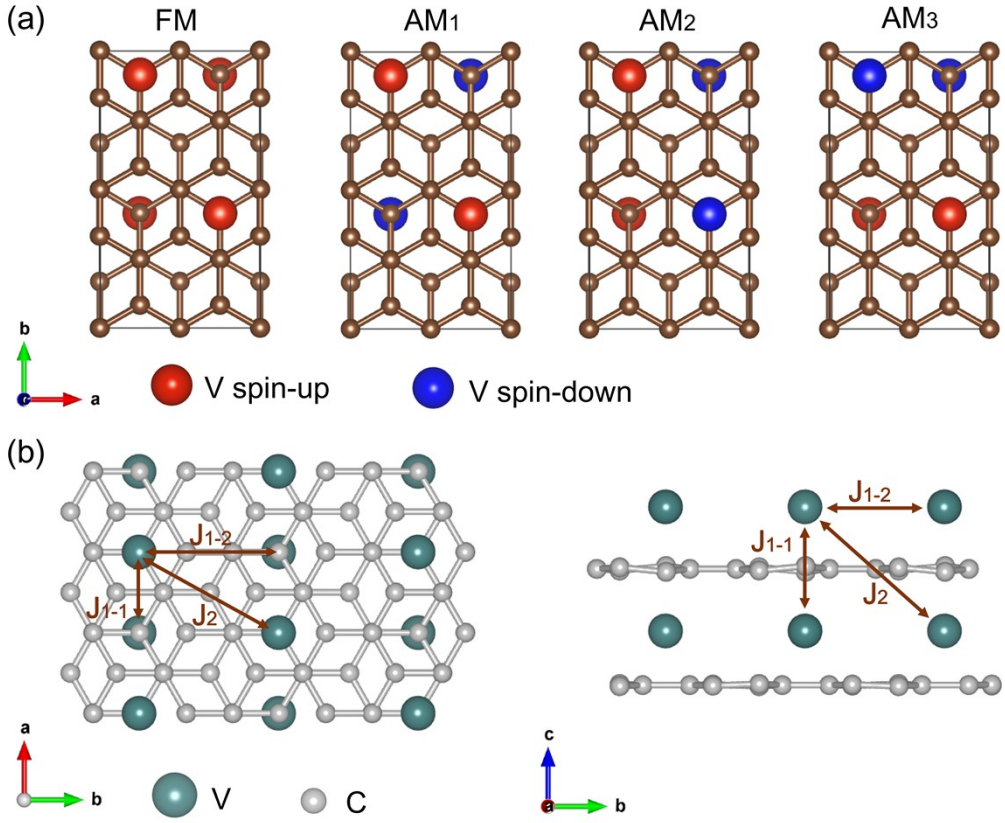

Fig. S7. (a) Supercells utilized for calculating exchange coupling constants in the NH structure. Brown spheres represent carbon atoms, and the red and blue spheres represent vanadium atoms with spin up and spin down. Energy differences among the four supercells were determined using DFT+*U* (U_{eff} = 5 eV). (b) Schematic representation of the magnetic exchange pairs in the NH structure.

To investigate the magnetic ground state and the corresponding exchange interactions of the NH phase, we calculated the total energies of four distinct magnetic configurations: FM, and three antiferromagnetic states (AM_1, AM_2, and AM_3). The corresponding supercell models and their spin-coupling schemes are illustrated in Fig. S6(a) and (b), respectively. By mapping these configurations onto the Heisenberg Hamiltonian, the energy of each state is expressed as:

$$E_{FM} = -E_0 - (4J_{1-1} + 4J_{1-2} + 6J_2)|\vec{S}|^2 - D|\vec{S}_z|^2$$
$$E_{AM1} = -E_0 - (-4J_{1-1} - 4J_{1-2} + 6J_2)|\vec{S}|^2 - D|\vec{S}_z|^2$$
$$E_{AM2} = -E_0 - (-4J_{1-1} + 4J_{1-2} - 2J_2)|\vec{S}|^2 - D|\vec{S}_z|^2$$
$$E_{AM2} = -E_0 - (4J_{1-1} - 4J_{1-2} - 2J_2)|\vec{S}|^2 - D|\vec{S}_z|^2$$

Our DFT results identify the AM_1 configuration as the magnetic ground state. Relative to the AM_1 state, the calculated energies for FM, AM_2, and AM_3 states are 0.62 eV, 0.92 eV and 0.50 eV, respectively. These energy differences allow for self-consistent determination of the exchange coupling constants J_{1-1}, J_{1-2}, and J_2 for the NH phase.

References

1 M. I. Aroyo, J. M. Perez-Mato, D. Orobengoa and E. Tasci.

2 X. Chen, J. Ren, Y. Zhu, Y. Yu, A. Zhang, P. Liu, J. Li, Y. Liu, C. Li and Q. Liu, *Phys. Rev. X*, 2024, **14**, 31038.

3 J.-C. Charlier, X. Gonze and J.-P. Michenaud, *Phys. Rev. B*, 1991, **43**, 4579–4589.